An Optical Sensor Designed From Cascaded Anti-Resonant Reflection Waveguide and Fiber Ring-Shaped Structure for Simultaneous Measurement of Refractive Index and Temperature

Jiewen Zheng, Bo Liu 🟢, Lilong Zhao, Rahat Ullah, Yaya Mao 🟢, Jianxin Ren 🟢, and Tutao Wang

Abstract—A novel optical fiber sensor based on cascade anti-resonant reflection waveguide (ARRW) and fiber ring-shaped structure (FRSS) is proposed and experimentally demonstrated for simultaneous measurement of refractive index (RI) and temperature. The sensor is very simply fabricated by splicing ARRW and FRSS based on Mach-Zehnder interference (MZI). The FRSS interference dip is sensitive to external RI and temperature changes, whereas the ARRW structure's loss dip is only sensitive to external temperature. As a result, this sensor can be used to measure both RI and temperature simultaneously. The sensor's maximum RI sensitivity is 108.61 nm/RIU and its maximum temperature sensitivity is 19 pm/ °C in the experiment. This sensor is a good choice when it is necessary to measure RI and temperature at the same time due to its compact size, high sensitivity, low cost, and good stability.

Index Terms—Anti-resonant reflection waveguide, fiber ring-shaped structure, RI measurement, temperature measurement.

I. INTRODUCTION

DUE to their unique advantages such as strong anti-electromagnetic interference ability, high sensitivity, good insulation, ease of manufacture, and corrosion resistance, optical fiber sensors have received a lot of attention in recent years. Accurate measurement of RI is needed in food, environment, and chemical industry. Up to now, many optical fiber RI sensors have been reported, including long-period fiber grating (LPFG) [1], Mach-Zehnder interferometers (MZI) [2], Michelson interferometers (MI) [3], Modal interferometer [4], Fabry-Perot interferometers (FPI) [5], and surface plasmon resonance [6],

[7]. Compared with these sensors, sensors made of curved single-mode fiber (SMF) [8], [9], based on the interference between the core mode and the whispering gallery mode (WGM) [10], are easier to realize by mechanical bending SMF without any professional equipment and more sensitive to RI.

However, all the above sensors are sensitive to temperature changes due of the inherent thermo-optic effect of optical fibers material. The temperature cross-sensitivity will reduce the measurement accuracy and limit the actual use when the sensor is used practically for measuring the change in RI. Therefore, simultaneous measurement of RI and temperature are of crucial importance for many biochemical and physical practical applications. Fiber gratings, such as (LPFG) and fiber Bragg gratings (FBG), are commonly used to measure RI and temperature simultaneously in a cascade with other sensing structures due to their temperature-sensitive and RI insensitive characteristics. These sensors are usually composed by cascading fiber gratings with another structure, such as special optical fiber [11], s-shaped taper [12], droplet-like fiber structure [13], core-offset MZI [14], microfiber knot resonators [15], etc., or by embedding another structure, abrupt tapered tip [16] and in-line MZI [17]. However, in the manufacturing process of these hybrid sensors, whether fiber gratings or other cascaded structures, complex preprocessing usually requires the use of expensive equipment, such as femtosecond lasers or high precision cutting equipment, all of which limit their development in large-scale production and practical applications. Therefore, the optical fiber interferometer structure and the reference structure with simple manufacturing process for simultaneous measurement will be extremely valuable. The ARRW structure [18]–[20] has the advantages of easy manufacture, compact structure, and low cost, and its working mechanism is different from that of MZI. Consequently, it shows great application potential in measuring RI and temperature simultaneously after cascading with other MZI structures.

In this article, the sensor designed from cascaded configuration of FRSS and ARRW for simultaneous measurement of RI and temperature is proposed for the first time. The structural configuration of the whole sensor is described in Fig. 1.(a). The sensor is designed by splicing a silica capillary tube (SCT) between two sections of SMF to form a sandwich structure
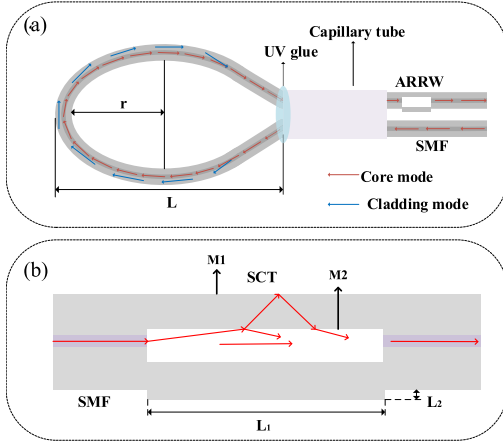
Fig. 1. (a) Schematic diagram of the proposed sensor based on cascade FRSS and ARRW; (b) The anti-resonant reflecting guidance mechanisms in the SCT.

Fig. 2. Transmission spectrum of the FRSS with different bending radius.

and then bending the SMF with the coating removed into a balloon shape with a section of capillary tube. The FRSS is used to measure the external RI, while the ARRW loss dip is used to as the reference spectrum dip and provide temperature compensation, allowing for simultaneous measurement of the RI and temperature. The maximum RI and temperature sensitivity of the sensor are 108.61 nm/RIU and 19.0 pm/°C. For each component of the proposed cascade sensor, whether FRSS or ARRW, they are easy to manufacture. The sensor has the ability to compensate for the temperature effect in the case of RI-based sensing and can be widely used in the fields of environmental, biological, and chemical sciences.

II. FABRICATION AND PRINCIPLE

A. Fiber Ring-Shaped Structure (FRSS)

As illustrated in Fig.1(a), the working principle of FRSS is based on the interference between the core mode and cladding mode. L and r are the maximum length and bending radius of FRSS, respectively. When light propagates from the introduced SMF to the FRSS, due to the mode field mismatch caused by fiber bending, some light in the core is excited into the cladding as the cladding mode, while another light continues to propagate in the core as the core mode. Due to the RI of the cladding is larger than surrounding environment, the WGM will be excited and propagate along the bending region [21]. Because of the standard symmetrical structure of FRSS, some cladding mode light is recoupled to the SMF core after propagating through the bending region symmetrical to the excitation point, and the cladding mode interferes with the central core mode due to the different optical path and the different RI between the core and cladding to form MZI. As a typical MZI, the output intensity of interference fringes can be expressed as [2]:

$$I = I_1 + I_2 + 2\sqrt{I_1 I_2} \cos \phi \quad (1)$$

where I_1 and I_2 are the light intensity of core mode and cladding mode; ϕ is the phase difference between the core mode and cladding mode. The interference dip occurs in the transmission spectrum under the following conditions:
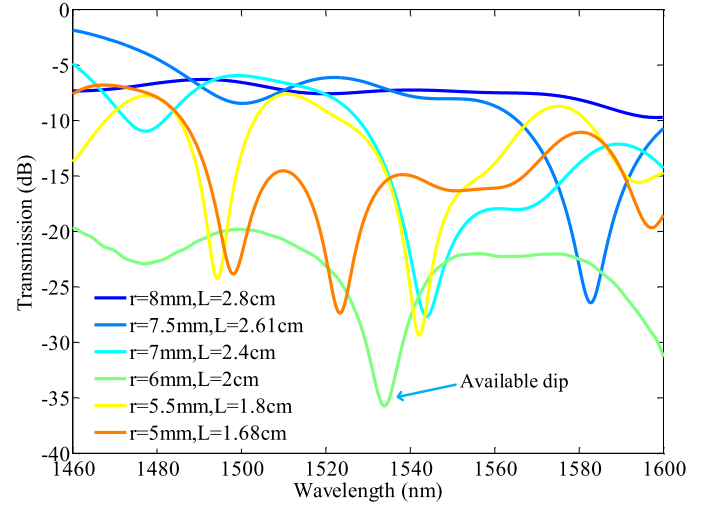
$$\phi = \frac{2\pi L_e}{\lambda} \Delta n_e \quad (2)$$

where L_e is the effective interference length, λ is the wavelength of incident light; $\Delta n_e = \Delta n_{e1} - \Delta n_{e2}$ is the effective RI difference between the core mode and cladding mode, where Δn_{e1} and Δn_{e2} are the effective RI of core mode and cladding mode, respectively. When the phase difference meets the conditions [22]:

$$\lambda_m = \frac{2L_e \Delta n_e}{2m + 1} \quad (3)$$

where m is an integer and λ_m is the wavelength of the *m-th* interference fringe.

The free spectral range(FSR) of this MZI can be given by:

$$FSR = \frac{\lambda_m^2}{L_e \Delta n_e} \quad (4)$$

It can be seen from (4) that the FSR of the FRSS decreases with the increase of the L_e. It should be noted that the L_e is not the length of the corresponding bending part, but the effective length that can stimulate WGM transmission. In general, the larger the bending radian of the optical fiber, the earlier WGM is excited into the cladding in the transmission process, which means that in the bending structure, a smaller r corresponds to a larger L_e. According to (3), changes in external temperature or RI result in changes in the values of Δn_e and L_e, resulting in the change of interference dip in the transmission spectrum. The feasibility of the FRSS for RI and temperature measurement is thus demonstrated in principle. To verify the above discussion of FRSS, the FRSS with different r is investigated experimentally,as shown in Fig. 2. Because most of the light remains in the core and is rarely excited into the cladding, there will be no interference dip in the wavelength range when r of FRSS is greater than 8mm, as shown in Fig. 2. As r decreases from 7.5 to 6 mm, available interference dip appears blue shift. The occurrence of more available interference dips means that the transmission
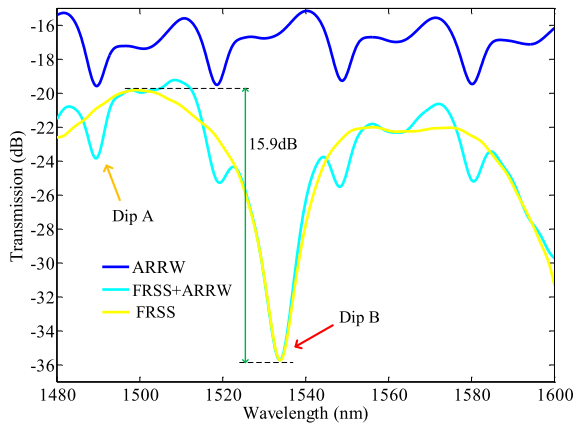
Fig. 3. The transmission spectrum of the single FRSS, the single ARRW, and the cascade structure.
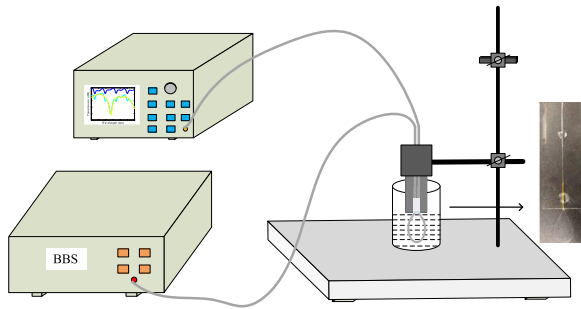

Fig. 4. Schematic diagram of the experimental setup for RI measurement.
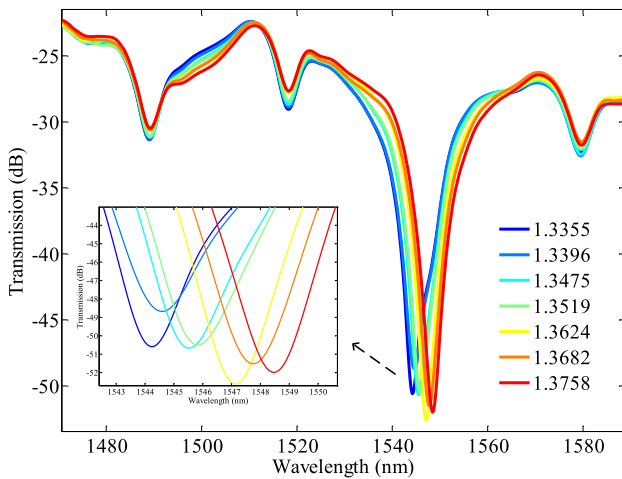

Fig. 5. The transmission spectrum evolution as RI is changed.

spectrum's FSR is reduced when r is further reduced to 5 mm. Furthermore, the extinction ratio of these interference dips decreases as r decreases. More light will be excited into the cladding as r decreases, and it may even leak from the cladding to the external environment, resulting in significant signal loss.

B. Anti-Resonant Reflection Waveguide (ARRW)

When the light passes through the end of FRSS, it is transmitted from the lead-in SMF to SCT. The classical ARRW model
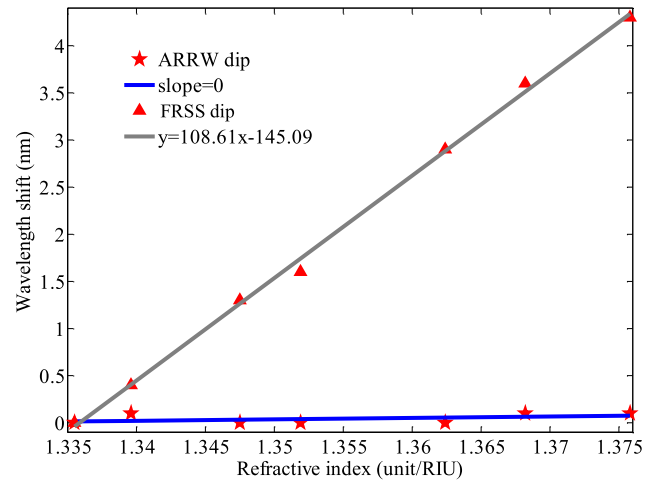

Fig. 6. Linear fitting curves of FRSS and ARRW dip wavelength shifts against RI variation.
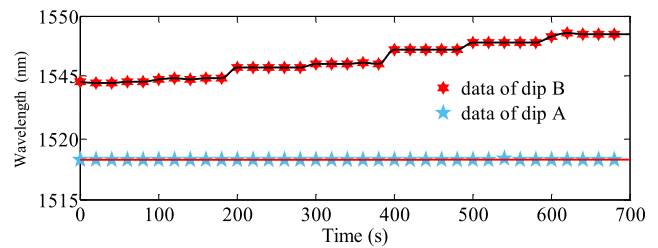
Fig. 7. The variation of the dip A and B with surrounding RI in the time domain.
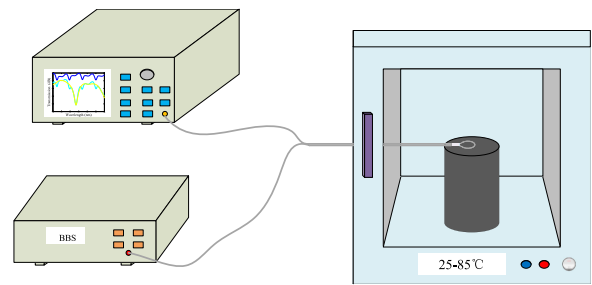
Fig. 8. Schematic diagram of the experimental setup for temperature measurement.

can be established to explain the transmission characteristics of light in SCT, as illustrated in Fig 1.(b). M2 and M1 are the inner and outer walls of the SCT. Along the radial direction, the ring cladding of SCT can be used as a F-P etalon. The light satisfying the resonance condition will not be reflected by the F-P etalon, which leads to periodic loss dip in the transmission spectrum of the etalon. On the contrary, the light that does not meet the resonance condition is internally reflected and confined in the SCT as the guiding mode. The position of the $m'-th$ transmission dip in the spectrum can be calculated as follows [19]:

$$\lambda_{m'} = \frac{2d}{m'} \sqrt{n_1^2 - n_{\text{air}}^2} \qquad (5)$$

TABLE I
COMPARISONS OF OPTICAL FIBER RI AND TEMPERATURE SENSORS BY DIFFERENT STRUCTURES AND THEIR PERFORMANCES

| Sensing Structure	RI/Temperature sensitivities	Probe type	Fabrication	Ref.
LPG+PCF	(171.96nm/RIU)/(47.4pm/°C)	No	Complicated	[6]
LPFG+S taper	(311.48nm/RIU)/(45.87pm/°C)	No	Complicated	[7]
FBG+Droplet-like Structure	(157.89nm/RIU)/(23.8pm/°C)	Yes	Complicated	[8]
MZI+FBG	(-101.3nm/RIU)/(100pm/°C)	No	Complicated	[25]
BFS+SMS	(331.71nm/RIU)/(1.053nm/°C)	Yes	Complicated	[26]
SMS+LPFG	(87nm/RIU)/(99.8pm/°C)	No	Complicated	[27]
FRSS+ARRW	(108.61nm/RIU)/(19pm/°C)	Yes	Easy	This work
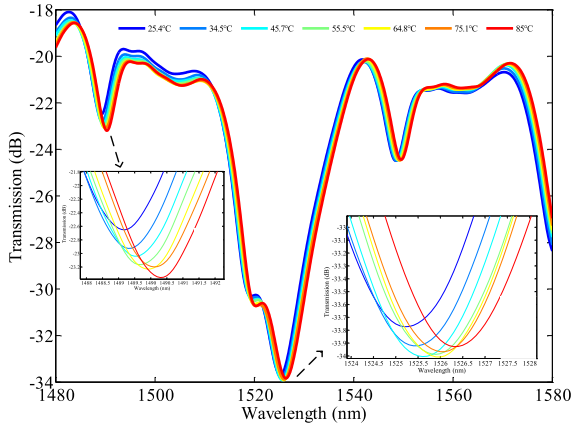
Fig. 9.   The transmission spectrum evolution as temperature is changed.

where $\lambda_{m'}$ is the $m'-th$ resonant wavelength; the thickness and RI of the cladding of the SCT to be d and n_1; n_{air} is the RI of air. For those wavelengths that satisfy the resonant condition, the transmission power can be expressed as [23]:

$$T_{ARROW} = \frac{(1 - R \cdot R')^2 (R + R')^2}{1 + R'^4 - 2R'^2} I_{Arrow} \qquad (6)$$

where I_{Arrow} is the intensity of input light at the resonant wavelength; the reflection coefficient of the inner and outer surface of the ring cladding to be R and R'.

Based on (5), the temperature sensitivity of ARRW can be deduced as:

$$\frac{\partial \lambda_{m'}}{\partial T} \approx \frac{2n_1 d}{m'\sqrt{n_1^2 - n_{air}^2}} \cdot \frac{\partial n_1}{\partial T} = \lambda_m \cdot \frac{n_1}{n_1^2 - n_{air}^2} \cdot \frac{\partial n_1}{\partial T} \qquad (7)$$

where $\partial n_1/\partial T$ (the thermal optical coefficient of silicon) is 1.1×10^{-5}/°C.

This sensor can be fabricated relatively straightforwardly and simple. Initially SCT with $L_1 = 1000$ μm was spliced between the lead-in SMF and lead-out SMF. The inner diameter and outer diameter of SCT are 150 μm and 75 μm, respectively. To make the obtained ARRW spectrum have an obvious loss dip, the lateral offset (L_2) of fusion SCT and SMF is 25 μm. Discharge time of 300 ms and arc power of -25bit can be adopted to avoid the collapsing of SCT by fusion splicer (Fujikura 80s). After removing the coating of lead-in SMF with a suitable length,

lead-in SMF and lead-out SMF are fixed into balloon-shaped by a capillary tube with the length of 1 cm and inner diameter of 400 μm. The r of FRSS can be adjusted as required by moving the ends of the lead-in SMF or lead-out SMF. After determining the optimal r, fix the FRSS on the glass sheet with ultraviolet (UV) glue. After fixing, the r of the sensor is 6 mm and the L is 2 cm. The transmission spectrum of FRSS alone is measured, as illustrated in Fig. 3 (yellow line). The desired dip was selected for sensing measurement since the available interference dip is located in the center of the wavelength range and has little effect on the dip of ARRW as shown in Fig. 3. In addition, it has a high extinction ratio of 15.9 dB. Moreover, the transmission spectra of ARRW (blue line) and cascade structure (green line) were recorded, as shown in Fig. 3.

Changes in L_e and Δn_e caused by external RI or temperature changes will move the interference dip of FRSS move.

Therefore, the FRSS is sensitive to both temperature and RI. For the ARRW, the external RI changes only act on FRSS as shown in Fig. 4. Therefore, it can be inferred that the dip generated by ARRW is only sensitive to temperature and not RI. The dip generated by ARRW can be used as a reference to provide temperature compensation for FRSS and to measure temperature and RI simultaneously. The wavelength changes of ARRW dip $\Delta\lambda_A$ and FRSS dip $\Delta\lambda_B$ caused by the ambient temperature and RI change can be calculated as [24]:

$$\Delta\lambda_B = k_{T_1} \cdot \Delta T + k_{N_1} \cdot \Delta N$$
$$\Delta\lambda_A = k_{T_2} \cdot \Delta T \qquad (8)$$

Where ΔT and ΔN respectively represent the changes of temperature and RI, k_{T_1} and k_{N_1} respectively represent the sensitivity of balloon dip to temperature and RI, k_{T_2} is the sensitivity of ARRW dip to temperature.

III. EXPERIMENTS AND RESULTS

A. For Analyzing the RI Response

The RI's experimental setup is depicted in Fig. 4. Fix the sensor-loaded glass sheet to the height-adjustable support splint. To record the transmission spectrum, a broadband light source (BBS) with a spectral range of 1440–1640 nm is connected to the sensor's lead-in SMF end, and an optical spectral analyzer
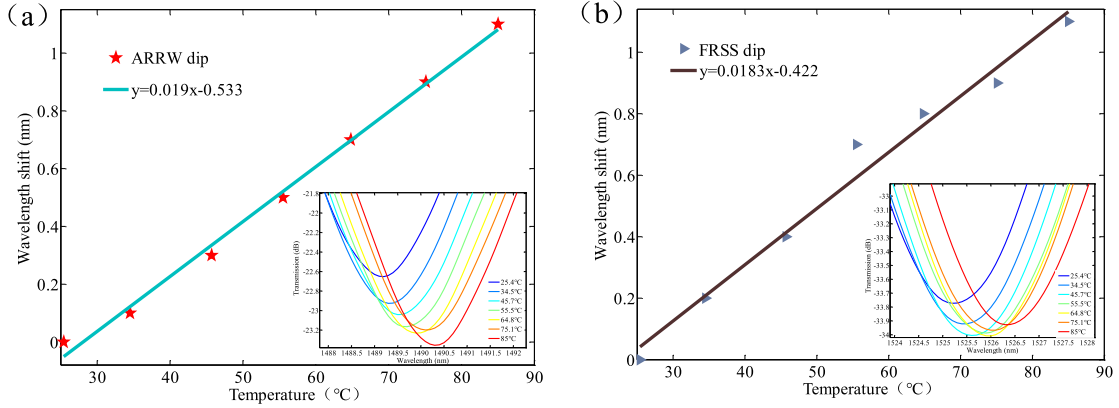
Fig. 10. Wavelength shift against surrounding temperature variation: (a) and (b) Linear fitting curve of ARRW dip and FRSS dip wavelength with temperature.

(OSA, YOKOGAWA, AQ6370D) is connected to the sensor's lead-out SMF end.

Fig. 5 depicts how the sensor transmission spectrum changes as the RI rises from 1.3355 to 1.3758 while the ambient temperature remains constant at 25 °C. The Fig. 5 shows that when the RI changes, the two independent dips show a different change in the characteristics. The FRSS dip shows a significant red shift, while the ARRW dip has no wavelength shift. By further linear fitting, the RI responses of dip A and dip B about wavelength were plotted, respectively, as shown in Fig. 6. The corresponding RI sensitivities of dip B was 108.61 nm/RIU. From the above experimental results, the ARRW dip is not sensitive to RI, which is consistent with the theoretical analysis.

To verify the repeatability and stability of the proposed sensor, we repeated five measurements at each RI and recorded the spectrum after each RI was maintained for 6 minutes. It can be seen from Fig. 7 that the evolution of dip wavelength with RI variation. It can be concluded from the results of repeated experiments that for each RI, both the dips of ARRW and FRSS remain basically unchanged, which shows that the proposed sensor has good stability and repeatability.

B. For Analyzing the Temperature Response

The temperature response of the proposed sensor was then analyzed. The input end of the sensor is connected to the BBS, and the output end is connected to the OSA, as illustrated in Fig. 8. Fix the glass sheet loaded with the sensor in the temperature controller (TC). The temperature of the TC increased from 25 °C to 85 °C with a step of 10 °C ± 0.5 °C. After waiting for 5 minutes at each temperature point to stabilize the temperature in TC, we recorded the evolution of the transmission spectrum, as illustrated in Fig. 9.

The temperature response of Dip A and Dip B were plotted as shown in the insert pictures in Fig.10(a) and (b). The ARRW dip and the FRSS dip moved toward a longer wavelength with the temperature increase from 25 °C to 85 °C. The corresponding wavelength sensitivities of the ARRW dip and the FRSS dip are 19 pm/°C and 18.3 pm/°C, respectively.

The response of the proposed sensor to RI and temperature is consistent with the theoretical analysis. FRSS is sensitive to both

temperature and RI, and since ARRW is sensitive to temperature but insensitive to RI, it can be used for temperature compensation to achieve the goal of simultaneous measurement of RI and temperature. After obtaining the sensitivity coefficients of the two sensing mechanisms, a demodulation matrix needs to be established to calculate the changes of temperature and RI, which can be given by:

$$\begin{bmatrix} \Delta N \\ \Delta T \end{bmatrix} = \begin{bmatrix} 0 & 19 \\ 108.61 & 18.3 \end{bmatrix}^{-1} \begin{bmatrix} \Delta \lambda_A \\ \Delta \lambda_B \end{bmatrix} \tag{9}$$

ARRW and FRSS must meet certain conditions for the proposed cascade structure to perform well in the simultaneous measurement of temperature and RI. The requirement for FRSS is that there is only one available dip, which has a high extinction ratio. In the experiment, we found that this condition can be satisfied when r is between 6 mm and 7.5 mm. The presence of an obvious insertion loss dip is a requirement of ARRW. Because the transmission spectrum of the ARRW has obvious available loss dips when the length of the SCT is between 500 μm and 2000 μm, precise control of the length of the SCT is less important. As can be seen from (7), there is no relation between SCT length (L_1) and temperature sensitivity. Therefore, even if the cutting accuracy of the common fiber cutting machine is not high, it can still be used in the manufacturing process of the sensor without affecting the performance of the cascade sensor, to realize quantitative production. For each component of the proposed cascade sensor, whether FRSS or ARRW, they are easy to manufacture. As shown in Table I, when compared with the reported cascade sensors for simultaneously RI and temperature sensing, the proposed sensor uses ARRW instead of FBG or LPFG to provide temperature compensation, so that the manufacturing of the whole sensor does not need high precision cutting equipment, so as to simplify the manufacturing process and reduce the manufacturing cost, making the sensor a good choice for industrial quantitative production.

IV. CONCLUSION

The sensor cascade of ARRW and FRSS is proposed and verified to realize dual-parameter measurement for the first time. The sensor is designed by splicing a SCT to a SMF, and then

fix the lead-in SMF and lead-out SMF into balloon-shaped by a capillary tube. Because the spectral dip of FRSS is sensitive to external RI and temperature change, ARRW is introduced to generate reference dip for accurate RI and temperature measurement. We can draw a conclusion from the experiment that the sensor has high RI and temperature sensitivity of 108.61 nm/RIU and 19 pm/°C, respectively. According to the sensitivity coefficient obtained by linear fitting, the solution modulation matrix is successfully established to realize the accurate measurement of RI and temperature simultaneously. The proposed sensor has high sensitivity, a small volume, and is simple to manufacture. It can be used in chemical manufacturing, medicine, and environmental monitoring.

REFERENCES

[1] J. Guo *et al.*, "Compact long-period fiber gratings with resonance at second-order diffraction," *IEEE Photon. Technol. Lett.*, vol. 24, no. 16, pp. 1393–1395, Jun. 2012.

[2] L. Sun *et al.*, "Ultra-high sensitivity of dual dispersion turning point taper-based Mach-Zehnder interferometer," *Opt. Exp.*, vol. 27, pp. 23103–23111, 2019.

[3] Z. Tian, S. S. Yam, and H. Loock, "Refractive index sensor based on an abrupt taper Michelson interferometer in a single-mode fiber," *Opt. Lett.*, vol. 33, pp. 1105–1107, 2008.

[4] S. Xiao *et al.*, "Simultaneous measurement of refractive index and temperature using SMP in Sagnac loop," *Opt. Laser Technol.*, vol. 96, pp. 254–258, 2017.

[5] B. Xu, Y. Yang, Z. Jia, and D. N. Wang, "Hybrid Fabry-Perot interferometer for simultaneous liquid refractive index and temperature measurement," *Opt. Exp.*, vol. 25, pp. 14483–14493, 2017.

[6] H. Zhang *et al.*, "Biosensing performance of a plasmonic-grating-based nanolaser," *Prog. Electromagnetics Res.*, vol. 171, pp. 159–169, 2021.

[7] H. Zhang *et al.*, "Quasi-BIC laser enabled by high-contrast grating resonator for gas detection," *Nanophotonics*, vol. 11, pp. 297–304, 2022, doi: 10.1515/nanoph-2021-0368.

[8] X. Zhang and W. Peng, "Bent fiber interferometer," *J. Lightw. Technol.*, vol. 33, pp. 3351–3356, 2015.

[9] X. Liu, Y. Zhao, R. Lv, and Q. Wang, "High sensitivity balloon-like interferometer for refractive index and temperature measurement," *IEEE Photon. Technol. Lett.*, vol. 28, no. 13, pp. 1485–1488, Apr. 2016.

[10] A. Harris and P. Castle, "Bend loss measurements on high numerical aperture single-mode fibers as a function of wavelength and bend radius," *J. Lightw. Technol.*, vol. 4, pp. 34–40, 1986.

[11] D. J. J. Hu *et al.*, "Long period grating cascaded to photonic crystal fiber modal interferometer for simultaneous measurement of temperature and refractive index," *Opt. Lett.*, vol. 37, pp. 2283–2285, 2012.

[12] J. Li *et al.*, "Long-period fiber grating cascaded to an S fiber taper for simultaneous measurement of temperature and refractive index," *IEEE Photon. Technol. Lett.*, vol. 25, no. 9, pp. 888–891, Mar. 2013.

[13] Y. Chen, Q. Han, T. Liu, F. Liu, and Y. Yunzhi, "Simultaneous measurement of refractive index and temperature using a cascaded FBG/Droplet-like fiber structure," *IEEE Sensors J.*, vol. 15, no. 11, pp. 6432–6436, Jun. 2015.

[14] Q. Yao *et al.*, "Simultaneous measurement of refractive index and temperature based on a core-offset Mach–Zehnder interferometer combined with a fiber Bragg grating," *Sensors Actuators A: Phys.*, vol. 209, pp. 73–77, 2014.

[15] Y. Xiao, X. Cai, and H. Chen, "Simultaneous measurement of temperature and refractive index based on microfiber knot resonators and FBGs," *Optik*, vol. 191, pp. 116–120, 2019.

[16] A. D. Gomes, B. Silveira, S. C. Warren-Smith, M. Becker, M. Rothhardt, and O. Frazão, "Temperature independent refractive index measurement using a fiber Bragg grating on abrupt tapered tip," *Opt. Laser Technol.*, vol. 101, pp. 227–231, 2018.

[17] F. Ahmed, V. Ahsani, A. Saad, and M. B. G. Jun, "Bragg grating embedded in Mach-Zehnder interferometer for refractive index and temperature sensing," *IEEE Photon. Technol. Lett.*, vol. 28, no. 18, pp. 1968–1971, Jun. 2016.

[18] W. Sun *et al.*, "Comparative study on transmission mechanisms in a SMF-Capillary-SMF structure," *J. Lightw. Technol.*, vol. 38, no. 15, pp. 4075–4085, 2020.

[19] S. Liu, J. Tian, N. Liu, J. Xia, and P. Lu, "Temperature insensitive liquid level sensor based on antiresonant reflecting guidance in silica tube," *J. Lightw. Technol.*, vol. 34, no. 22, pp. 5239–5243, 2016.

[20] R. Gao, D. Lu, J. Cheng, Y. Jiang, L. Jiang, and Z. Qi, "Optical displacement sensor in a capillary covered hollow core fiber based on anti-resonant reflecting guidance," *IEEE J. Sel. Topics Quantum Electron.*, vol. 23, no. 2, pp. 193–198, May 2017.

[21] L. Xu *et al.*, "High-Q silk fibroin whispering gallery microresonator," *Opt. Exp.*, vol. 24, no. 18, pp. 20825–20830, 2016.

[22] P. Chen, X. Shu, and K. Sugden, "Ultra-compact all-in-fiber-core Mach-Zehnder interferometer," *Opt. Lett.*, vol. 42, no. 42, pp. 4059–4062, 2017.

[23] S. Liu, Y. Wang, M. Hou, J. Guo, Z. Li, and P. Lu, "Anti-resonant reflecting guidance in alcohol-filled hollow core photonic crystal fiber for sensing applications," *Opt. Exp.*, vol. 21, no. 25, pp. 31690–31697, 2013.

[24] B. Xu, Y. M. Liu, D. N. Wang, and J. Q. Li, "Fiber Fabry–Pérot interferometer for measurement of gas pressure and temperature," *J. Lightw. Technol.*, vol. 34, pp. 4920–4925, 2016.

[25] W. Zhang, W. Gao, Z. Tong, Y. Zhong, L. Xue, and H. Zhang, "Mach–Zehnder interferometer cascaded with FBG for simultaneous measurement of RI and temperature," *Opt. Commun.*, vol. 466, 2020, Art. no. 125624.

[26] Y. Hu *et al.*, "Simultaneous measurement of the refractive index and temperature based on a hybrid fiber interferometer," *IEEE Sensors J.*, vol. 20, no. 22, pp. 13411–13417, Jun. 2020.

[27] J. Huang, X. Lan, A. Kaur, H. Wang, L. Yuan, and H. Xiao, "Temperature compensated refractometer based on a cascaded SMS/LPFG fiber structure," *Sensors Actuators B: Chem.*, vol. 198, pp. 384–387, 2014.